INTERNATIONAL JOURNAL OF ROBUST AND NONLINEAR CONTROL
Int. J. Robust Nonlinear Control 2005; **0**:1–0 *Prepared using* rncauth.cls *[Version: 2002/11/11 v1.00]*

A robust integrated controller/diagnosis aircraft application

Andrés Marcos[1]*and Gary J. Balas[2]

[1] *Post-Doctoral Fellow, University of Leicester, Leicester, LE2 2LG, UK*
[2] *Professor, University of Minnesota, Minneapolis, Minnesota 55455, USA*

SUMMARY

In this paper, an application of the robust integrated control/diagnosis approach using $\mathcal{H}_\infty$-optimization techniques to the nonlinear longitudinal dynamics of a Boeing 747-100/200 aircraft is presented. The integrated approach allows to address directly the trade-off between the conflicting controller and fault diagnosis objectives. The integrated design formulation (interconnection and weight selection) is defined using five LTI plants obtained through out the Up-and-Away flight envelope. Linear and nonlinear closed-loop time simulations are carried out under a realistic turbulence and noise environment. A comparison drawn with the non-integrated design of a controller and a diagnosis filter with the same objectives shows that the integrated case results in similar diagnosis characteristics but improved fault tolerant performance and ease of design.

KEY WORDS: Fault tolerant systems, fault diagnosis, robust integrated controller

1. Introduction

The integrated design of a controller and a diagnosis filter for an uncertain system is known to have several advantages with respect to their independent (non-integrated) design. Specifically, the trade-off between the controller and the filter conflicting objectives (i.e. robustness of the controller versus performance of the diagnosis filter) can be addressed directly in the integrated case. It is known that this conflict between the design of the controller and the filter stems from coupling of the respective objectives when uncertainty is present, see references [10, 14, 21]. Furthermore, the integrated framework facilitates the incorporation of fault tolerant characteristics in the controller.

Reference [10], first proposed and studied an integrated controller/diagnosis design approach, the four-parameter controller, in order to address this conflict. In reference [19], the integrated

*Correspondence to: A. Marcos, Department of Engineering, Control & Instrumentation Group, University of Leicester, Leicester, LE2 2LG, UK. Telephone: +44-116-252-2874, Fax: +44-116-252-2619, E-mail: ame12@le.ac.uk.

Contract/grant sponsor: NASA Langley Cooperative Agreement, Technical contract monitor Dr.Christine Belcastro; contract/grant number: NCC-1-337

Received 24-March-2005

approach was casted in a general framework and solutions were provided based on optimal and robust theory. The previous two references were further developed in [14] which proposed solutions in terms of the standard robust control configuration [22] for nominal and uncertain systems. Reference [21] proposed a mixed $\mathcal{H}_2/\mathcal{H}_\infty$ criterion to design a reconfigurable control with optimized control and diagnostic performance indexes. Furthermore, integrated fault tolerant and residual generation architectures, based on the Youla and the Dual Youla parameterizations for high-performance controllers [18], have also appeared recently in a breadth of papers, see references [17, 16, 23, 6]. Although the underlying synthesis technique for all the previous approaches is the well-known $\mathcal{H}_\infty/\mu$ optimization, only several applications of the robust integrated approach are available in the literature [19, 17, 15, 1] and none, to the best of our knowledge, pertaining aerospace systems or comparing the design to the non-integrated case.

In this paper, the applicability of the integrated design using $\mathcal{H}_\infty$-optimization techniques and its comparison with the non-integrated design for a nonlinear aerospace system, i.e. the longitudinal motion of a Boeing 747-100/200 aircraft, is shown. The integrated design formulation (interconnection and weight selection) is carried out for linear time-invariant (LTI) plants obtained at five equilibrium points through out the Up-and-Away flight envelope of the Boeing 747-100/200 aircraft. The same interconnection structure and weights are used for all the LTI models in order to assess the robustness of the designs and the possibility of gain-scheduling the five LTI integrated controllers to cover the entire flight envelope. Closed-loop time simulations are carried out for the LTI plants and also for the full nonlinear equations of motion of the aircraft, i.e. longitudinal and lateral, under a realistic turbulence and noise environment to validate the design.

The layout of the paper is as follows. Section 2 briefly introduces the integrated approach. The nonlinear and linear models are described in Section 3. Section 4 presents the problem formulation and controller/diagnosis objectives. The analysis of the resulting designs is presented in Section 5. The comparison with the non-integrated filter design and controller from references [7, 4] is also provided in Section 5. Conclusions are given in Section 6.

2. Theory

It is well-known [14, 11] that the design of a feedback controller and a diagnostic filter can be carried out independently for a nominal plant but that for the uncertain case, their design is coupled through the uncertainty in the plant. The integrated control/diagnosis filter approach attempts to solve the conflict arising from this uncertainty coupling by providing a common mathematical formulation where the opposing objectives are traded-off in the initial steps of the design process. In the case of $\mathcal{H}_\infty$-optimization, the integrated controller synthesis consists of the definition of a common interconnection for the controller and the filter, and the selection of proper weighting functions for the trade-off of the different performance and robustness objectives.

The mathematical formulation of the problem, i.e. the selection of the error channels and their interconnection, is problem dependent but can be described generally based on the four-parameter controller from references [9, 10]. The four-parameter controller is a generalization of the Youla parameterization which extends the standard feedback controller to four degrees of freedom (DoF): reference signal tracking, closed-loop stabilization, residual generation, and

disturbance rejection. Theorem 2.1 provides a general parameterization result for the four-parameter controller, see also Figure 1.

Theorem 2.1 (General Four-parameter Controller) *Consider a nominal plant $G_u \in \mathcal{R}_P$ (the space of real-rational, and proper functions). Assume a corresponding nominal stabilizing controller $K_o \in \mathcal{R}_P$ and feedforward controller $K_{ff} \in \mathcal{R}_P$ are given. Let any right/left coprime factorizations (r.c.f./l.c.f) for the nominal plant, $G_u = N_u M^{-1} = \tilde{M}^{-1}\tilde{N}_u$, and the controllers, $K_o = UV^{-1} = \tilde{V}^{-1}\tilde{U}$ and $K_{ff} = U_{ff}V^{-1} = \tilde{V}^{-1}\tilde{U}_{ff}$, be known. The class of all proper integrated (stabilizing and residual generator) controllers $K_F(Q) \in \mathcal{R}_P$ is parameterized by:*

$$\begin{bmatrix} u \\ r_w \end{bmatrix} = \begin{bmatrix} (\tilde{V} + Q_c\tilde{N}_u)^{-1}(\tilde{U} + Q_c\tilde{M}) & (\tilde{V} + Q_c\tilde{N}_u)^{-1}(\tilde{U}_{ff} + Q_{cw}) \\ Q_f\left(\tilde{M} - \tilde{N}_u(\tilde{V} + Q_c\tilde{N}_u)^{-1}(\tilde{U} + Q_c\tilde{M})\right) & Q_{fw} - Q_f\tilde{N}_u(\tilde{V} + Q_c\tilde{N}_u)^{-1}(\tilde{U}_{ff} + Q_{cw}) \end{bmatrix} \begin{bmatrix} y \\ w \end{bmatrix} \tag{1}$$

Under the following conditions: $(\tilde{V} + Q_c\tilde{N}_u)(\infty)$ exist and

$$\begin{bmatrix} s \\ r_w \end{bmatrix} = Q \begin{bmatrix} \tilde{r} \\ w \end{bmatrix} = \begin{bmatrix} Q_c & Q_{cw} \\ Q_f & Q_{fw} \end{bmatrix} \begin{bmatrix} \tilde{r} \\ w \end{bmatrix} \in \mathcal{RH}_\infty, \tag{2}$$

where u is the feedback control input, r_w the residual vector, y the plant measurements and $w = cmd$ the exogenous input. The internal signals s and $\tilde{r}$ are respectively the contribution of the Youla parameters to the feedback controller and the primary residual.

Proof: The proof, based on Theorem (33) in reference [9] and Theorem 12.17 from [22], can be obtained in reference [5].

Remark 1. For the above parameterization of $K_F(Q)$, the coprime factor $\tilde{V}$ has been assumed the same in the feedforward, $K_{ff} = \tilde{V}^{-1}\tilde{U}_{ff}$, and the feedback controller, $K_o = \tilde{V}^{-1}\tilde{U}$. This is due to the well-known requirement that K_{ff} be stable or if unstable, implemented together with the feedback controller. Note that in Figure 1, the term $\tilde{V}$ is not apparent but can be obtained by using the parameterization given in equation (1).

Remark 2. The controller parameterization of equation (1) is an adaptation, but equivalent (after setting $\tilde{U}_{ff} = 0$ and some direct manipulations), to the formulae given in [9, 10]. The class of four-parameter controllers is associated with the implicit internal model principle, i.e. its parameterization contains a model of the plant. This association is highlighted by the internal signal $\tilde{r}$ which is called the primary residual and is equal to:

$$\tilde{r} = \tilde{M}y - \tilde{N}_u u \tag{3}$$

From this primary residual signal it is also easy to see the connection with the residual generation theory. The parameterization of all residual generators for a system $y = G_u\ u + G_d\ d + G_f\ f$ can be given in terms of a free-parameter $Q_f \in \mathcal{RH}_\infty$ [3]. Introducing the fault and disturbance signals $[f^{\mathrm{T}}\ d^{\mathrm{T}}]^{\mathrm{T}}$, the residual vector r can be generated using the following frequency-domain residual generator:

$$r = Q_f\ \tilde{r} = Q_f\ (\tilde{M}\ y - \tilde{N}_u\ u) = Q_f\ (\tilde{N}_f\ f + \tilde{N}_d\ d) \tag{4}$$

Note that for the nominal case, the residual generator cancels the effect of the inputs to the monitored system. The different FDI approaches are basically based on the diverse ways available to select the transfer functions $Q_f, \tilde{N}_f, \tilde{N}_d$ such that conditions on detectability,

isolability, identification of faults, and filter performance are fulfilled, see reference [2]. Also, notice that in the general case of the four-parameter controller the diagnostic signal r_w equals the residual from equation (4) corrected by a term due to the exogenous input influence, i.e. $(Q_{fw}\ w)$.

Remark 3. Removing the second row of the integrated controller from equation (1), corresponding to the diagnostic signal generation, the well-known two degrees-of-freedom controller parameterization from [20] is obtained. Furthermore, the term K_{11} corresponds to the feedback controller Youla parameterization. A detailed analysis of the transfer function constraints and algebraic limitations with respect to nominal performance, robust stability and other closed-loop properties for the integrated approach is given in references [10, 14].

The weighting of the channels is quite heuristic and highly problem dependent, as in all $\mathcal{H}_\infty$-optimization based techniques, but insight is obtained by qualitatively analyzing the purpose of the four general channels:

1. closed-loop stabilization, $K_{11} = TF_{y\to u}$: this is the standard output feedback control channel. The selected output of the plant y and control signal u are used to synthesize the desired feedback controller.

2. feedback reference signal tracking and disturbance rejection, $K_{12} = TF_{w\to u}$: In the case the signal w is obtained from a pre-defined ideal command reference model, the corresponding minimization of the transfer function implies signal tracking. If on the other hand, w signifies external disturbances, the transfer function minimization corresponds to a disturbance rejection objective.

3. residual generation, $K_{21} = TF_{y\to r_w}$: this transfer function is used to generate the desired residual diagnostic signals r_w based on the plant outputs y. Notice, that this is a generalization of the primary residual, equation (3), and as such it accounts indirectly for the plant inputs u as well.

4. diagnostic fault signal tracking and disturbance rejection, $K_{22} = TF_{w\to r_w}$: as with the term K_{12}, these two objectives are achieved depending on the definition of the signal w. For fault signal tracking, instead of an ideal command system an ideal fault reference model is defined based on the information and assumptions relative to the faults to be detected.

3. Models and environment

The model used for this application is a Boeing 747 series 100/200 aircraft. The Boeing 747 aircraft is an inter-continental wide-body transport with four fan jet engines designed to operate from international airports. The nonlinear model of the aircraft given in [7], including the set of aerodynamic coefficients, is used in the nonlinear simulations to assess the robustness and performance of the integrated controllers while LTI longitudinal motion models are used in the design stage.

The nonlinear body-axes longitudinal motion of the Boeing 747, not including flexible modes

or wind effects, can be described by the following differential equations [7, 13]:

$$\dot{\alpha} = \frac{[-F_x\ s_\alpha + F_z\ c_\alpha]}{m\ V_{TAS}} + q \tag{5}$$

$$\dot{q} = c_7\ M_y \tag{6}$$

$$\dot{\theta} = q \tag{7}$$

$$\dot{V_{TAS}} = \frac{1}{m}\ [F_x\ c_\alpha + F_z\ s_\alpha] \tag{8}$$

$$\dot{he} = V_{TAS}\ c_\alpha\ s_\theta - V_{TAS}\ s_\alpha\ c_\theta\ =\ V_{TAS}\ sin\gamma \tag{9}$$

The longitudinal states are angle of attack α (rad), pitch rate q (rad/sec), true velocity V_{TAS} (m/sec), pitch angle θ (rad), and altitude he (m). The aerodynamic forces along the X and Z-axis and the pitching moment are given by F_x, F_z and M_y respectively. The inertial coefficient is given by $c_7 = 1/I_{yy}$ $(1/\text{Kg}/m^2)$ and the cosine and sine by c_α and s_θ. The aerodynamic forces and moments are defined in terms of dimensionless aerodynamic coefficients $(C_D, C_L, C_Y, C_l, C_m, C_n)$, flight dynamic pressure $\bar{q}$ (N/m^2), reference area S (m^2), and in the case of the moments, the moment-arm (either wing chord $\bar{c}$ (m), or wing span b (m)). The aerodynamic coefficients are provided as look-up tables (LUT) function of a wide set of parameters (angle of attack, true airspeed, sideslip angle, and altitude among others). See reference [7] for a detailed presentation of the nonlinear terms (i.e. F_x, F_z, M_x and $C_D, C_L, C_Y, C_l, C_m, C_n$).

The longitudinal motion LTI models are obtained through Jacobian linearizations of the nonlinear model at different points in the flight envelope of interest ($he \in$ [4000,10000] m, $Vtas \in$ [150,250] m/sec). Table I shows the trim points in the flight envelope used for design. The LTI models have five states : pitch rate q (rad/s), true airspeed V_{TAS} (m/sec), angle-of-attack α (rad), pitch angle θ (rad), and altitude he (m). There are two control inputs: elevator deflection δ_e (rad) and the combined thrust for the four engines Tn (N). The measurements available are flight path angle γ (rad), normal acceleration in g's $\dot{V}/g$ (non-dim), pitch angle θ (rad), pitch rate q (rad/s), velocity V_{TAS} (m/sec), and altitude he (m). The state-space LTI plant at design point 1 in Table I is given by:

$$A = \begin{bmatrix} -5.7754e^{-1} & -2.7297e^{-4} & -1.8125 & 0 & -2.7377e^{-6} \\ -1.4634e^{-1} & -7.0744e^{-3} & 4.7328 & -9.7942 & 5.3951e^{-5} \\ 9.8597e^{-1} & -7.2473e^{-4} & -6.6013e^{-1} & -3.0087e^{-18} & 5.1464e^{-6} \\ 1 & 0 & 0 & 0 & 0 \\ 0 & -6.9389e^{-18} & -1.8400e^{2} & 1.8400e^{2} & 0 \end{bmatrix}; \quad B = \begin{bmatrix} -1.5580 & 1.5328e^{-7} \\ 3.7706e^{-15} & 1.3304e^{-5} \\ -3.9056e^{-2} & -5.7220e^{-9} \\ 0 & 0 \\ 0 & 0 \end{bmatrix};$$

$$C = \begin{bmatrix} 0 & 0 & -1 & 1 & 0 \\ -1.4922e^{-2} & -7.2139e^{-4} & 4.8261e^{-1} & -9.9873e^{-1} & 5.5014e^{-6} \\ 0 & 0 & 0 & 1 & 0 \\ 1 & 0 & 0 & 0 & 0 \\ 0 & 1 & 0 & 0 & 0 \\ 0 & 0 & 0 & 0 & 1 \end{bmatrix}; \qquad D = \begin{bmatrix} 0 & 0 \\ 3.8450e^{-16} & 1.3567e^{-6} \\ 0 & 0 \\ 0 & 0 \\ 0 & 0 \\ 0 & 0 \end{bmatrix};$$

The deflection and rate limits for the elevator are -23 to 17 deg and ± 37 deg/s respectively. Taking the rate limits into account, the elevator is modeled as a simple first-order transfer function: $act_{\delta_e} = 37/(s+37)$. The engine dynamics are modeled as $act_{eng} = 0.5/(s+0.5)$.

The closed-loop simulations are corrupted by noise in the sensors and by a turbulence model. Turbulence is simulated by feeding white noise, through stable and minimum-phase spectra

filters, to the system. There are several analytical functions which provide turbulence spectra, see reference [8], but the Dryden spectra is selected in this application. For the longitudinal (symmetric) and lateral (asymmetric) motions of an aircraft in turbulence, the model developed at Delft University of Technology is followed [8]. This model simulates turbulence in the nonlinear aircraft model by feeding the output of the Dryden filters directly through the stability derivatives. This is non-standard, typically the aircraft velocity states are corrected by wind-turbulence components and these are used to determined the adequate forces and moments, but by directly correcting the stability derivatives a more specific nonlinear effect is obtained. Coloring filters are used in the simulation to achieve a realistic level of noise in the sensor measurements. The sensor dynamics are modeled using low-pass filters. See reference [5, 7] for more details in the turbulence and sensor models.

4. Integrated controller/diagnosis design

The design of an $\mathcal{H}_\infty$-optimization controller is characterized by two basic steps: the selection of the interconnection (problem formulation) and the choice of appropriate weights (optimization objectives formulation). The integrated design (from now on, referred to as integrated controller as well) for the Boeing 747-100/200 aircraft is carried out for five LTI plants obtained at five equilibrium points through out the Up-and-Away flight envelope of the aircraft, see Table I. The same interconnection structure and weights are used for all the LTI models in order to assess the robustness and the possibility of gain-scheduling the five LTI integrated designs to cover the entire flight envelope.

The control objectives are to achieve de-coupled tracking of flight path angle command γ_c and velocity command $Vtas_c$ with settling times of 15 sec and 45 sec respectively [4]. These performance characteristics are assuming fully functional actuators and sensors. Furthermore, the controller should be robust to model uncertainty and should reject gust disturbances for the Up-and-Away flight envelope. In the case of faults in the elevator actuator and/or pitch rate sensor, the closed-loop should be able to maintain stability and performance (the latter possibly degraded if the severity of the fault becomes critical). Hence, it is required to design a robust fault tolerant controller with good performance characteristics for the nominal case.

The diagnosis objectives are to detect and isolate faults in the elevator actuator and the pitch rate sensor [7]. The diagnostic channels should be decoupled from the commands and from each other, be robust to model uncertainty and plant variations, and be able to reject or attenuate disturbances (gust, noise, ...).

A model-matching formulation is used to track the desired commands (velocity and flight path angle) and to provide diagnostic of the desired faults (pitch rate sensor and elevator). Furthermore, the control objectives are achieved by using a two-degree controller formulation. The faults are assumed to enter the system in an additive manner: e.g. the elevator deflection to the plant δ_{ele} is equal to the actuator deflection $act_{\delta_{ele}}$ plus the fault f_{act}. The final interconnection is given in Figure 2.

The exogenous inputs to the interconnection are the *noise* vector (one channel per LTI plant output), the command signals $(\gamma_{cmd}, Vtas_{cmd})$, and the fault signals (f_{act}, f_{sen}). The interconnection exogenous outputs are the error channels for the control and the diagnosis objectives: $e_c = [\gamma_{error} \quad Vtas_{error}]^{\mathrm{T}}$ and $e_f = [act_{error} \quad sen_{error}]^{\mathrm{T}}$. The measurements available to the integrated controller are the difference between the flight path angle command

and its output $(\gamma_{cmd} - \gamma)$, the rest of the plant outputs $(\dot{V}/g, \theta, q, Vtas, he)$, and the velocity command $Vtas_{cmd}$. The integrated controller outputs are four: two signals for feedback control, $K_{\delta_{ele}}$ and K_{Tn}, and two diagnosis signals, res_{act} and res_{sen}. There are two input uncertainty channels corresponding to the two feedback control signals.

Since the formulation of the problem is based on model-matching, ideal models for the control Wid_c and diagnosis Wid_f signals are used. For each objective, the ideal models are given in a block diagonal format, e.g. $Wid_c = diag(Wid_\gamma, Wid_{Vtas})$. The ideal transfer function for the flight path angle response Wid_γ is modeled as a second-order system having a cut-off frequency at 0.35 rad/sec and a damping factor of 1, see equation (10). The settling time for this model is approximately 20 seconds (corresponding to a bandwidth of 0.22 rad/sec). For the ideal velocity model Wid_{Vtas}, a second-order model is also used with a settling time of 45 seconds. This is accomplished using a natural frequency of 0.15 rad/sec and the same damping factor as before to obtain a bandwidth of 0.1 rad/sec approximately, see equation (11). These ideal models are taken from reference [4]. An input scaling weight W_{scl} is used to normalize the command signals. The weight is selected as $diag(2, 7)$ corresponding to 2 degrees of γ_{cmd} and 7 m/sec for the $Vtas_{cmd}$.

$$Wid_\gamma = \frac{0.35^2}{s^2 + 2{\cdot}0.35{\cdot}1 + 0.35^2} \qquad Wid_{act} = 2\frac{\frac{s}{300} + 1}{\frac{s}{2} + 1} \tag{10}$$

$$Wid_{Vtas} = \frac{0.15^2}{s^2 + 2{\cdot}0.15{\cdot}1 + 0.15^2} \qquad Wid_{sen} = \frac{\frac{s}{300} + 1}{s + 1} \tag{11}$$

The ideal models for the faults are selected assuming a quite fast and reliable identification of the fault at low to mid range frequencies to avoid critical damage. Hence, the ideal model for the actuator fault Wid_{act} has a bandwidth around 2 rad/sec, while the sensor fault ideal model Wid_{sen} has a bandwidth of 1 rad/sec approximately, see equations (10-11).

Error weights are used to specify the performance objectives for the control $W_{c_{error}}$ and the diagnosis objectives $W_{f_{error}}$ (as before with the ideal weights they are given in diagonal format respectively for each set of objectives). These weights define the overall characteristics of the integrated design: e.g. bandwidth requirements, steady-state requirements, attenuation/amplification of signals at certain frequency ranges, and de-coupling of the performance objectives. Its selection is based in an analysis of the plant dynamics (e.g. position of poles and zeros), and the interaction of these weights with the noise weights and the effect on the $\mathcal{H}_\infty$-optimization. Insight on their choice is given later in Section 5. The final selected weights are:

$$We_\gamma = \frac{\frac{s}{5} + 1}{\frac{s}{0.1} + 1} \qquad We_{act} = \frac{\frac{s}{5} + 1}{\frac{s}{0.001} + 1} \tag{12}$$

$$We_{Vtas} = 1.5\frac{\frac{s}{100} + 1}{\frac{s}{0.05} + 1} \qquad We_{sen} = \frac{\frac{s}{10} + 1}{\frac{s}{0.1} + 1} \tag{13}$$

The performance error weights for the control objectives We_γ and We_{Vtas} are scaled back at the output by the inverse of the scaling weight W_{scl} in order to preserve the input-output relation (this inverse weight is embedded in $W_{c_{error}}$ in Figure 2).

An input multiplicative uncertainty model is used to improve the robustness characteristics of the design. Typically, these uncertainty weights are used to limit the controller bandwidth

and allow for increasing model error at higher frequencies. In this formulation, a constant uncertainty weight provided sufficient uncertainty and reduced the number of states of the interconnection (and hence of the final integrated controller). Wu is a diagonal weight, one channel for each plant input, both constants of 0.1 magnitude corresponding to 10 percent uncertainty.

The last weights in the interconnection correspond to output disturbances. These weights are used to provide closed-loop robustness and represent noise in the system. In Figure 2, the weight Wn is a diagonal matrix with one entry for each of the plant outputs. The selection of the individual noise weights is typically performed selecting an acceptable level of noise and frequency range for each channel (based on the type of sensor and measurement). For example, the altitude, velocity and normal acceleration noise weights are selected as first order weights with the bandwidth dependent on the characteristics of the measurement (very slow for the altitude and faster dynamics for the velocity and acceleration) and a chosen level of noise in tune with their corresponding magnitudes:

$$Wn_\gamma = \frac{0.01}{57.3} \qquad Wn_{\dot{V}} = 0.1\frac{\frac{s}{0.5}+1}{\frac{s}{100}+1} \tag{14}$$

$$Wn_\theta = \frac{0.05}{57.3} \qquad Wn_q = \frac{0.01}{57.3} \tag{15}$$

$$Wn_{Vtas} = 0.05\frac{\frac{s}{0.5}+1}{\frac{s}{100}+1} \qquad Wn_{he} = \frac{\frac{s}{0.01}+1}{\frac{s}{150}+1} \tag{16}$$

5. Integrated controller/diagnosis analysis

Five LTI $\mathcal{H}_\infty$ integrated designs are synthesized using the previous weights and interconnection, each design corresponds to one of the five equilibrium points from Table I. A closed-loop $\mathcal{H}_\infty$-norm of 1.4142 is obtained for all the designs. The controllers have 20 states, 7 inputs, and 4 outputs. For brevity, only the analysis of the integrated controller designed at the nominal equilibrium point, point 1 ($he = 4000$ m, $Vtas = 184$ m/sec), is presented.

In cases where the order of the controller is such that it becomes an issue for implementation there are several techniques available to reduce it (e.g. Hankel state reduction, model truncation, ...). Although these order-reduction techniques sometimes result in degraded closed-loop performance, there are alternative $\mathcal{H}_\infty$-based approaches that result in lower-order controllers and have been successfully flight tested [12]. In this case no effort was made to reduce the integrated controller since hardware-in-the-loop was not attempted.

It is well-known that $\mathcal{H}_\infty$ techniques have no guarantees with respect to the stability of the controller. An unstable controller could also stabilize the closed-loop system but for practical reasons is typically not acceptable, hence the stability of the controllers is checked and found satisfactory. Furthermore, $\mathcal{H}_\infty$ controllers tend to have very fast poles (tending to infinity for the optimal case) which slow down the time-domain simulations thus residualization is sometimes used in practice. In the present case, there is no need since the fastest pole of the controller is around 50 radians/seconds.

Figure 3 shows the integrated controller transfer functions from all its inputs ($\gamma_c - \gamma, \dot{V}/g$, $\theta, q, Vtas, he$) to the feedback-control output channels ($K_{\delta_{ele}}$ and K_{Tn}). It is first noted that as expected the transfer functions of those input measurement channels typically affected by the engine thrust, i.e. velocity $Vtas$ and normal acceleration $\dot{V}/g$, show higher gain for K_{Tn} than for $K_{\delta_{ele}}$ (those primarily affected by the elevator show a higher gain for $K_{\delta_{ele}}$). Second, the transfer function from pitch angle to elevator channel, $TF_{\theta \to K_{\delta_{ele}}}$, clearly shows zeros and high gain at high frequencies. This will result in the control-part of the integrated controller being more sensitive to fast variations in θ during time simulations and is translated into high bandwidth for the elevator control-output resulting in fast oscillations of the control signal (but considered within limits). It is possible to reduce the high gain of the θ channel, for example by increasing the corresponding noise weight DC gain which tends to reduce the elevator control-output bandwidth and hence the high frequency variations due to the pitch angle. Unfortunately, more stringent weights, and hence lower gains for the θ channel, were associated with (more critical) loss of performance for the γ tracking objective and thus the present weights were kept.

Figure 4 shows the integrated controller transfer functions from all its inputs to the diagnosis output channels, i.e. to the actuator residual res_{act} and the pitch sensor residual res_{sen}. The transfer functions from the inputs to the actuator residual-output res_{act} and those to the elevator control-output $K_{\delta_{ele}}$ (from Figure 3) are almost identical up to a frequency of 1 radians/second. This is expected since the actuator fault to be detected enters the plant through the elevator channel (additive fault model) and thus shares the same frequency content at the low to mid frequency range. The second residual res_{sen} is used to diagnose faults in the pitch rate sensor, hence the associated transfer function for that particular channel, $TF_{q \to res_{sen}}$, presents higher DC gain than the transfer function to the actuator residual, $TF_{q \to res_{act}}$. Indeed, in all the other plots in Figure 4 the transfer functions corresponding to the res_{act} present higher gains.

In Figure 5, the sensitivity S and complementary sensitivity T functions for the control and diagnosis channels are shown. From left to right and top to bottom, the following transfer functions are plotted: $\gamma_{cmd}, Vtas_{cmd}$, actuator fault f_{act}, and sensor fault f_{sen} (each to their respective output and error). The plots show very good results for T and S (i.e. the sum of their magnitudes is about one, $T + S = 1$, and the magnitude is one at frequencies below cross-over for T and one at frequencies above it for S). Although not shown due to space limitations, no remarkable coupling between the two commands is observed. The only exception is a small peak of the $Vtas_{cmd}$ on the γ_{error} but at relatively high frequency compared to the γ bandwidth. Since the velocity is considered a very slow state, this coupling is considered negligible.

Even though the integrated approach addresses the coupling between control and diagnosis, there is still some coupling between the diagnostic channels which is analyzed in the next figure. This coupling could be reduced by further working on the selection of the weights or using additional residual evaluation schemes but the actual level of coupling is deemed small for the present research purposes. Figure 6 shows the unweighted interconnection transfer functions of the main channels that result in coupling on the fault residuals. The top plot is for the elevator fault residual res_{act}, and the bottom plot for the sensor residual res_{sen}. It is observed that as expected (see previous figures and comments), the θ channel results in coupling on both fault residuals, observe $TF_{\theta \to res_{act}}$ vs $TF_{f_{act} \to res_{act}}$ and $TF_{\theta \to res_{sen}}$ vs $TF_{f_{sen} \to res_{sen}}$, although with a higher gain (and hence influence) for the actuator residual.

The actuator residual (top plot in Figure 6) also suffers coupling due to the sensor fault

$TF_{f_{sen}\to res_{act}}$, the flight path command $TF_{\gamma_{cmd}\to res_{act}}$, and from the pitch rate transfer function $TF_{q\to res_{act}}$ (the latter frequency response is identical to that of the sensor fault $TF_{f_{sen}\to res_{act}}$). The high frequency coupling from q will be shown later to have adverse consequences for incipient (small) actuator fault diagnosis. With respect to the sensor residual transfer functions (bottom plot in Figure 6), the pitch rate to the sensor residual $TF_{q\to res_{sen}}$, is also identical to that from the sensor fault $TF_{f_{sen}\to res_{sen}}$. This is expected as the sensor fault enters in additive manner through the pitch rate channel, but it also means that actuator faults affecting the pitch rate will also show up on the sensor residual (although small since the coupling between the residuals, $TF_{f_{sen}\to res_{sen}}$ vs $TF_{f_{act}\to res_{sen}}$, is negligible). No other noticeable coupling is observed for the sensor residual.

The nominal performance NP, robust stability RS, and robust performance RP of the weighted closed-loop is examined next. The μ-analysis is performed assuming full complex uncertainty blocks representing unmodeled dynamics. For the 'total' integrated controller, by this it is meant that the control and diagnostic channels are all considered together, it is obtained (not shown) that at frequencies below 10^{-3} and 10^{-6} radians/seconds the nominal and robust performance degrade up to a magnitude of 1.01 and 1.3 respectively (e.g. the RP levels out at a magnitude of 1.3 at frequencies below 10^{-6} radians/seconds). This very-low frequency degradation of the performance is due to interactions between the plant and the control/diagnostic objectives (i.e. due primarily to the actuator fault but also to the γ command). This is observed in Figure 7 where the μ-analysis is performed independently for the control outputs ('control analysis' given in left plot) and for the diagnostic outputs ('filter analysis' in the right plot). The μ-analysis for the diagnostic channels (right plot) shows similar NP and RP to the 'total' controller analysis, while that for the control channels (left plot) yields better results with the robust performance settling at 1.01 at frequencies below 10^{-6} radians/seconds and the nominal performance a little less than 1.0. Better bounds could be obtained by sacrificing actuator and γ performance, but for the current problem formulation the results shown here are considered satisfactory.

To summarize, the integrated designs presents good decoupling, frequency behaviour, and robustness properties for the 'control' part implying that the control objectives in the time domain will be satisfied. With respect to the 'diagnostic' part, it is noted that the sensor residual also shows good decoupling from the other channels (except for some minor θ coupling) while the actuator residual is affected by variations in θ and q which indicate that this residual will be less robust but within acceptable limits (as shown next in the time simulations).

5.1. Time simulations

The final evaluation of the integrated control/diagnosis is carried out using linear and nonlinear time simulations. The LTI simulations (not shown, see [5] for details) show that the fault estimation and the command tracking are very good. The detection time (settling-time for the diagnosis) is 3 and 4 seconds for the actuator and sensor fault respectively. There is little coupling on the residual signals from the commands or the plant measurements, hence the decoupling objective for the fault estimates is achieved in the LTI case (which is expected as there is no uncertainty in this case). The settling times for the commands are 20 seconds for the γ command, and 40 seconds approximately for the velocity (by design they were selected to be around 20 and 45 seconds respectively). The velocity is more robust, with respect to the faults, than the γ channel. The elevator actuator fault results in some coupling in γ although

very small, i.e. fast transient with a magnitude of 0.1 degrees for almost a 3 degree abrupt fault in the elevator. This was expected based on the frequency-domain analysis.

Closing the loop with the nonlinear system enables evaluation of the designs for robustness to model uncertainty. The same manoeuvre and faults described in reference [7, 5] are used as a baseline test. The flight profile results in an aircraft manoeuvre that moves sufficiently far away from the initial equilibrium point in order to evaluate the size of the neighborhood around which the designs are valid. The manoeuvre selected is a steadily accelerated climb performed by commanding a 3 degree squared command for the flight path angle γ_{cmd} from t= 15 to t= 95, and a velocity step command of 18 m/sec starting at time = 20 seconds. The faults are clearly shown in Figure 8 by the dashed line, and correspond to 50 to 140 percent the nominal actuator magnitude (e.g. a nominal deflection of 1 degree will suffer and additive fault of 0.5 – 1.4 degrees) and up to 300 percent the nominal pitch rate for the sensor fault. This convoluted set of fault inputs is introduced to analyze couplings between the faults and the commands. It is unlikely a succession of faults as the one chosen will happen in the real system but each of the assumed faults is physically meaningful, i.e. they can represent stuck or constant-bias actuators and sensors (degradation and ramp-type faults were also tested and detected, see [5]). The disturbance rejection characteristics of the integrated designs are tested using the turbulence model and noisy sensors described in Section 3.

The noisy environment simulation is analyzed first. The initial flight condition selected for the noisy closed-loop nonlinear time simulations corresponds to the design point number five in Table I. Figure 8 shows the fault residuals under this noisy environment. As expected the sensor residual signal does a better job rejecting the disturbances, while the actuator residual is more sensitive to these disturbances. This was discussed in Section 5 based on the frequency response from Figure 6. Nevertheless, the actuator residual unmistakably diagnoses the elevator fault. The actuator residual res_{act} shows a detection time of 3 seconds. A small coupling due to the γ command (and its associated channel θ) is hardly observed. The sensor fault residual res_{sen} detects the fault in 4 seconds. The level of noise present in the elevator residual, $\pm$ 0.2 degrees, might prevent the detection of small incipient actuator faults but these faults are not critical at that magnitude (the elevator limits are +17/-23 degrees). In any case, a residual evaluation stage could suffice to provide a more desirable level of incipient fault detection.

Figure 9 shows the corresponding plant inputs and outputs. Very good disturbance rejection properties are observed for the commands. The tracking objectives are satisfied with a settling time of 35 seconds for the γ channel and close to 50 seconds for the velocity (slightly higher than for the LTI simulation but still within the desired limits). Decoupling between the commands is also quite remarkable with no discernible effects. The velocity also shows no coupling due to the faults while the flight path angle γ shows small transients due to the actuator fault (same as for the LTI case). As noted before, this fault coupling on γ comes from the fault effect on the elevator deflection and the transmission of these effects onto the pitch rate and pitch angle states, see the peaks in Figure 9. The pitch rate and elevator channel show also high frequency effects due to the noise, a level of $\pm$ 0.2 degrees. These effects are acceptable but it is noted that by the coupling of q on the actuator residual, see again Figure 6, they are transmitted to the actuator residual resulting in the afore mentioned level of missed incipient faults.

In order to analyze the behaviour of the different LTI $\mathcal{H}_\infty$ integrated controllers, Figure 10 shows the nonlinear closed-loop residual and command responses without gust or noise at the nominal flight condition, point 1, and two other extreme flight conditions, points 3 and 5. It is observed that for the sensor residual, the three $\mathcal{H}_\infty$ LTI designs show exactly the

same characteristics. The actuator residual is less robust with different levels of steady-state error for each of the designs. The nominal flight condition (he=4000 m, Vtas=184 m/sec) is given by the thick solid line and presents a maximum steady-state error of 6 percent; flight condition 3 (he=9250 m, Vtas=125 m/sec) is given by the thick dashed line and shows the largest error, approximately 25-30 percent of constant bias; the last flight condition, point 5 (he=7000 m,Vtas = 241 m/sec) is given by the dashed dot line and shows an error similar to the nominal flight condition but slightly more transient influence by the γ_{cmd}. The command responses show almost identical type of behaviour for all the designs. These results mean that the designs are all very robust to plant variations with only the actuator residual requiring minor corrections as the altitude and velocity change, possibly only gain changes scheduled on these two parameters.

5.2. Comparison of the integrated and the non-integrated designs

In order to conclude the integrated controller evaluation, a comparison is drawn with the non-integrated (independently designed) controller and diagnosis filter from references [7, 4]. The non-integrated controller (for lack of better name) was synthesized to provide good decoupling and tracking characteristics for the flight path angle and the velocity. It was designed to be robust to uncertainty but no direct effort was made to consider faults in the $\mathcal{H}_\infty$ formulation, see [4]. Hence, the non-integrated controller represents a fault-passive tolerant system able to handle non-critical faults (i.e. which can be considered as large disturbances). The non-integrated filter was designed after the non-integrated controller and it was tuned (quite time consuming) to provide good robustness and performance for the five selected trim conditions from Table I, see [7]. In the case of the integrated control/filter design, it has been seen that both objectives, diagnosis and control, are combined in the formulation. This results in a simpler and much faster design (although it must be noted that we built on the expertise acquired designing the non-integrated controller and filter). As noted in Section 2, this leads to a better trade-off between the controller and the diagnosis objective by the optimization.

Figure 11 shows the nonlinear responses (without noise or turbulence) comparison of the integrated and non-integrated designs for the design point 5. Only the residual and command plots are shown since similar plant inputs and outputs are obtained to those given in Figure 9. The residuals for both designs are very similar: they have a similar detection time and the level of coupling is similar as well. The command tracking performance objectives are also quite identical for both of them except that sensor faults affect much more the flight path angle response for the non-integrated case. This sensor fault coupling affects the performance of the non-integrated controller quite drastically although only in a transient way, see the peaks in the bottom plot.

It is remarked that the non-integrated controller was designed without direct fault considerations, i.e. a fault-passive controller, hence it is not surprising that slightly more abrupt faults result in the above performance degradation on the tracking objectives. Nevertheless, this comparison showcases that the integrated design enabled us to design a controller with the same performance characteristics but better robustness to faults by directly considering their effects in the formulation.

6. Conclusions

In this paper an application of the integrated control/diagnosis filter using $\mathcal{H}_\infty$-optimization has been presented for the nonlinear longitudinal motion of a Boeing 747-100/200 aircraft. Several integrated controller/diagnosis designs were synthesized using LTI plants at different flight conditions. The $\mathcal{H}_\infty$ LTI integrated designs were validated through time simulations using a nonlinear model of the aircraft. The results show that the integrated design has good performance and robustness characteristics for the control and diagnosis objectives.

Compared to the non-integrated design (independent design of the controller and the diagnosis filter), the integrated formulation reduces the time and simplifies the design task. It is noted that the reduction in time was partly due to the accumulated experience from the non-integrated designs but also due to the integrated formulation of the problem which enables the $\mathcal{H}_\infty$-optimization to automatically take care of the trade-off between the controller robustness and the diagnosis performance. The integrated design also improves fault tolerant control design by directly accounting for the faults in the problem formulation.

REFERENCES

1. Cardoso, A. and Dourado, A. Synthesis of a Robust Controller and Fault Detection Filter for an Unstable System. In *3rd IFAC symposium on Robust Control Design - ROCOND 2000*, Prague, Czech Republic, June 2000.
2. Chen, J. and Patton, R.J. *Robust Model-Based Fault Diagnosis for Dynamic Systems*. Kluwer Academic Publishers, 1999.
3. Ding, X. and Frank, P.M. Fault Detection via Factorization Approach. *Systems and Control Letters*, 14:431–436, 1990.
4. Ganguli, S., Marcos, A., and Balas, G.J. Reconfigurable LPV Control Design for Boeing 747-100/200 Longitudinal Axis. In *American Control Conference*, volume 5, pages 3612 –3617, Anchorage, AK, May 2002.
5. Marcos, A. *Aircraft Applications of Fault Detection and Isolation Techniques*. PhD thesis, Department of Aerospace Engineering and Mechanics, University of Minnesota-Minneapolis, Minneapolis,MN, February 2004.
6. Marcos, A. and Balas, G.J. Linear Fractional transformation of the Integrated Controller Approach. In *UK Control 2004 Conference*, Bath, UK, September 2004.
7. Marcos, A., Ganguli, S., and Balas, G.J. Application of $\mathcal{H}_\infty$ Fault Detection and Isolation to a Boeing 747-100/200 Aircraft. In *AIAA Guidance, Navigation, and Control Conference, AIAA-2002-4944*, Monterey, CA, August 2002.
8. Mulder, J.A. and van der Vaart, J.C. Aircraft Responses to Atmospheric Turbulence. Technical Report Lectures Notes D-4, Delft University of Technology, Delft, The Netherlands, 1998.
9. Nett, C.N. Algebraic aspects of linear control system stability. *IEEE Transactions on Automatic Control*, 31(10):941–949, Oct 1986.
10. Nett, C.N., Jacobson, C.A., and Miller, A.T. An Integrated Approach to Controls and Diagnostics: the 4-Parameter Controller. In *American Control Conference*, pages 824–835, 1988.
11. Niemann, H. and Stoustrup, J. Integration of control and fault detection: Nominal and robust design. In *IFAC Safeprocess '97*, pages 341–346, Hull, UK, August 1997.
12. Prempain, E. and Postlethwaite, I. Static H-infinity Loop Shaping Control of a Fly-By-Wire Helicopter. In *IEEE Conference on Decision and Control*, Bahamas, December 2005.
13. Stevens, B. and Lewis, F. *Aircraft Control and Simulation*. John Wiley & Sons, Inc., 2 edition, 1992.
14. Stoustrup, J., Grimble, M.J., and Niemann, H. Design of integrated systems for the control and detection of actuator/sensor faults. *Sensor Review*, 17 (2):138–149, July 1997.
15. Stoustrup, J. and Niemann, H. Application of an $\mathcal{H}_\infty$ Based FDI and Control Scheme for the Three Tank System. In *IFAC Symposium on Fault Detection, Supervision and Safety for Technical Processes*, pages 268–273, June 2000.
16. Stoustrup, J. and Niemann, H. Fault Tolerant Feedback Control. In *ECC, Porto, Portugal*, pages 1970–1974, September 2001.

17. Suzuki, T. and Tomizuka, M. Joint Synthesis of Fault Detector and Controller Based on Structure of Two-Degree-of-Freedom Control System. In *IEEE Conference on Decision and Control*, pages 3599–3604, Phoenix, AZ, Aug 1999.
18. Tay, T.T., Mareels, I., and Moore, J.B. *High Performance Control*. Birkhauser, 1998.
19. Tyler, M.L. and Morari, M. Optimal and Robust Design of Integrated Control and Diagnostic Modules. In *American Control Conference*, pages 2060–2064, Baltimore, MD, June 1994.
20. Vidyasagar, M. *Control System Synthesis: A Factorization Approach*. MIT Press, Cambridge, Massachusetts, 1985.
21. Wu, N.E. Robust Feedback Design with Optimized Diagnostic Performance. *IEEE Transactions on Automatic Control*, 42(9):1264 –1268, Sept 1997.
22. Zhou, K., Doyle, J.C., and Glover, K. *Robust and Optimal Control*. Prenticel-Hall, Englewood Cliffs, NJ, 1996.
23. Zhou, K. and Ren, Z. A New Controller Architecture for High Performance, Robust, and Fault-Tolerant Control. *IEEE Transactions on Automatic Control*, 46(10):1613–1618, 2001.

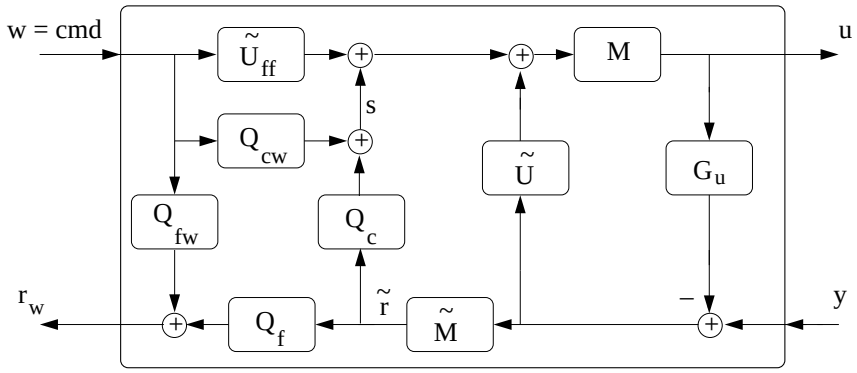

Figure 1. Four-parameter controller parameterization structure.

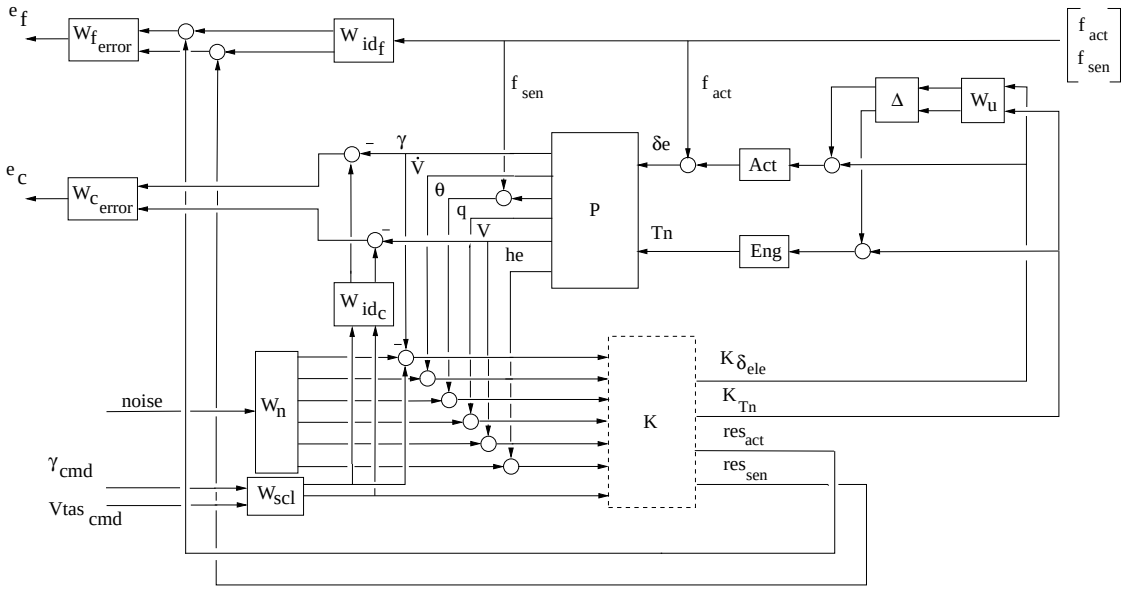

Figure 2. Integrated controller interconnection.

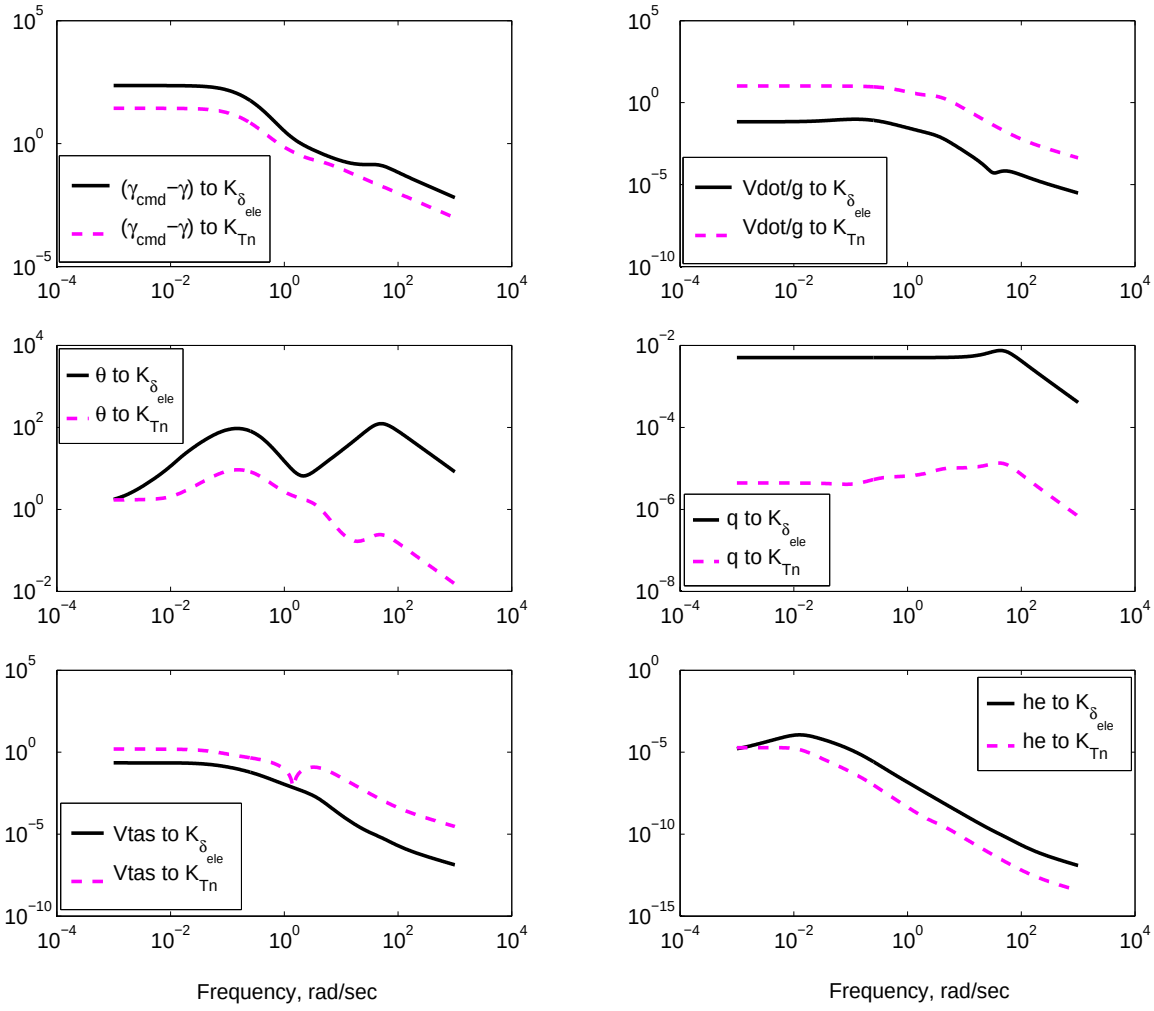

Figure 3. Integrated controller: inputs to control outputs.

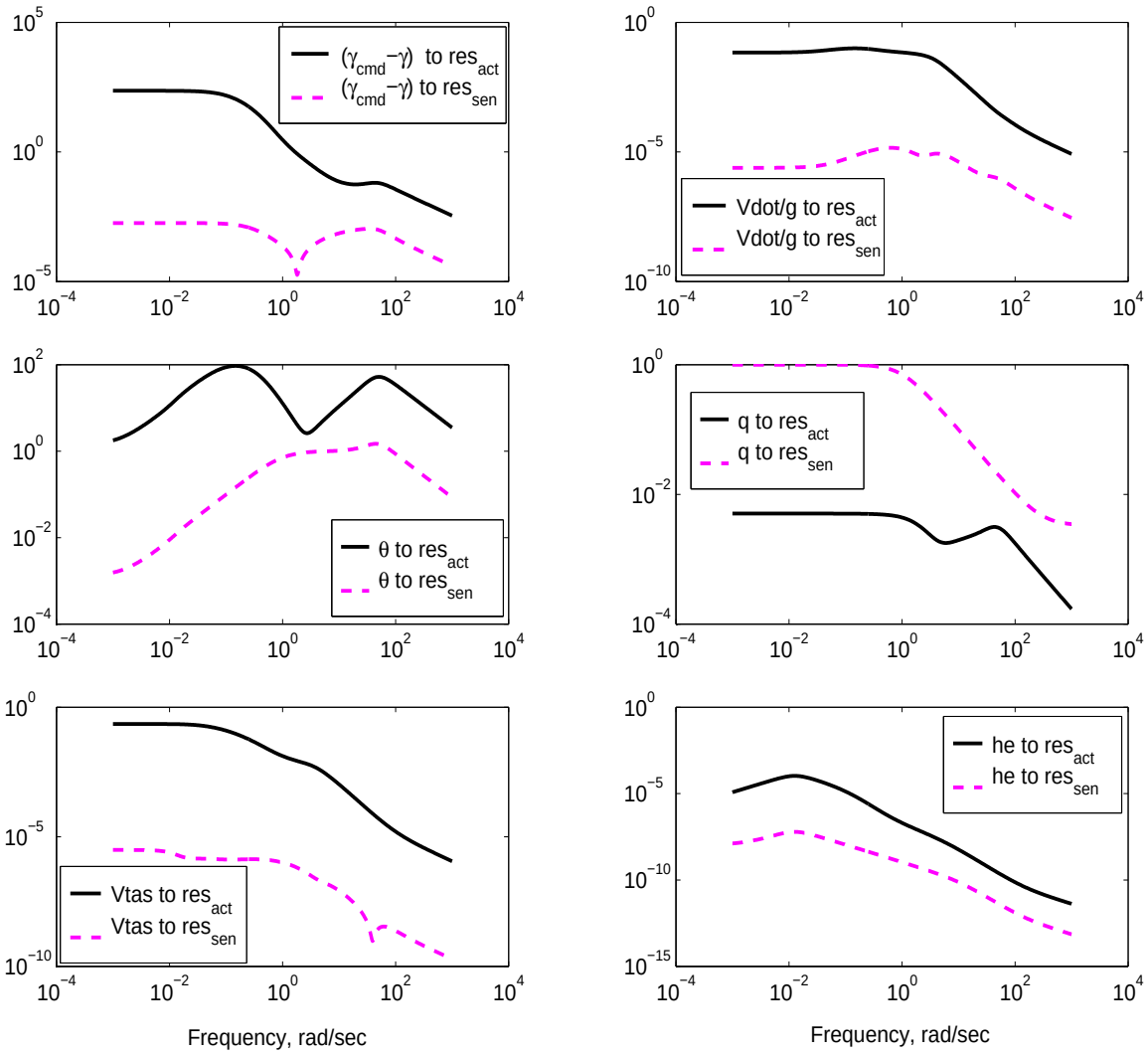

Figure 4. Integrated controller: inputs to diagnosis outputs.

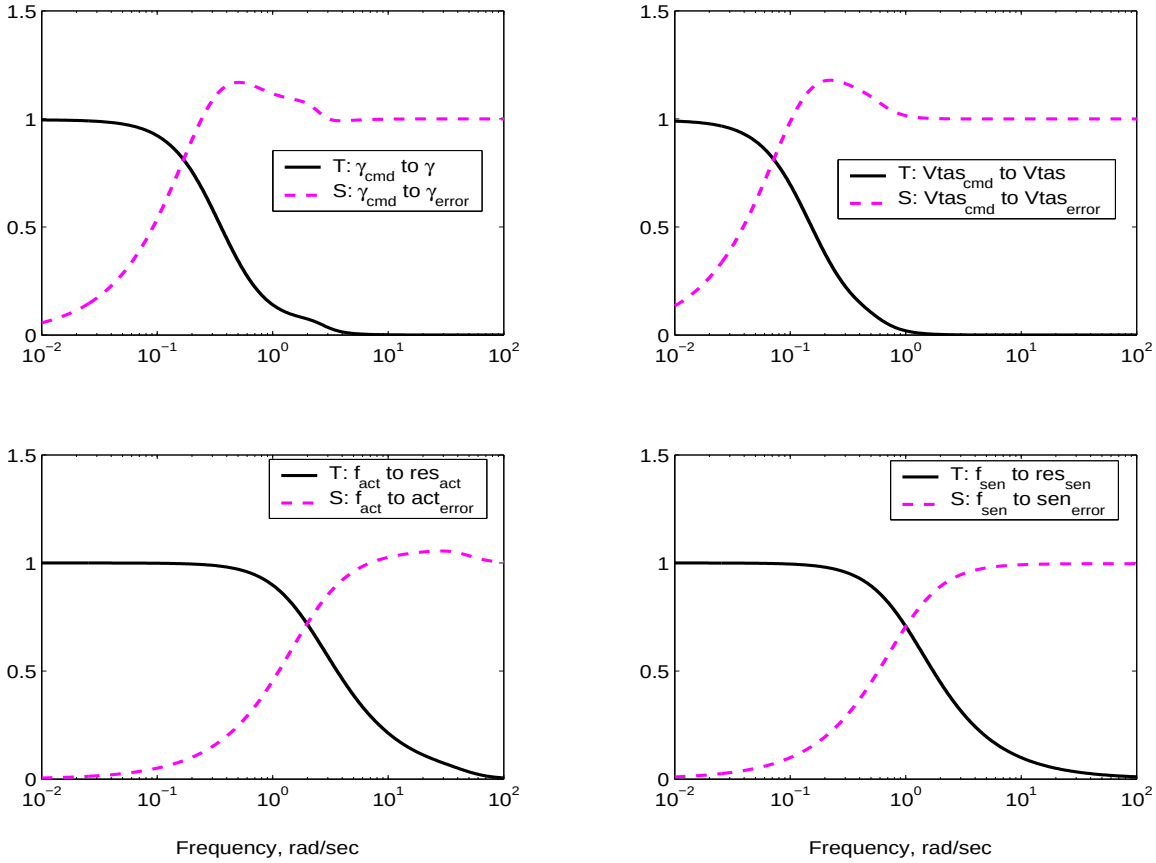

Figure 5. Unweighted closed-loop system: T and S.

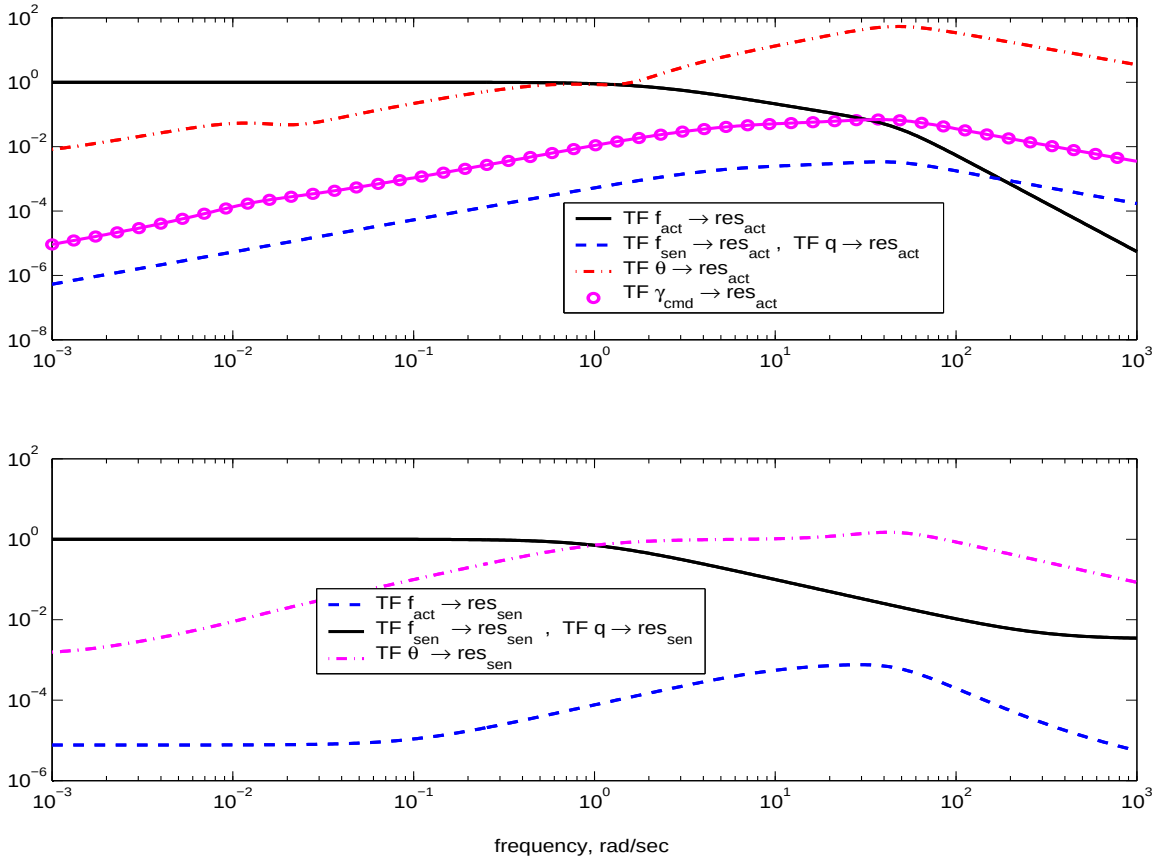

Figure 6. Transfer functions disturbances and commands to residuals.

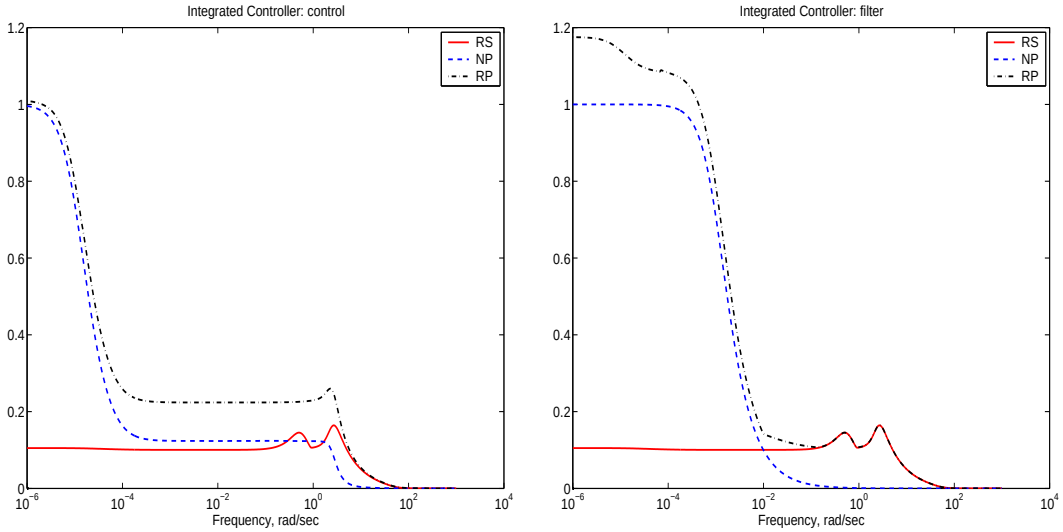

Figure 7. Weighted closed-loop: μ analysis filter/control controller.

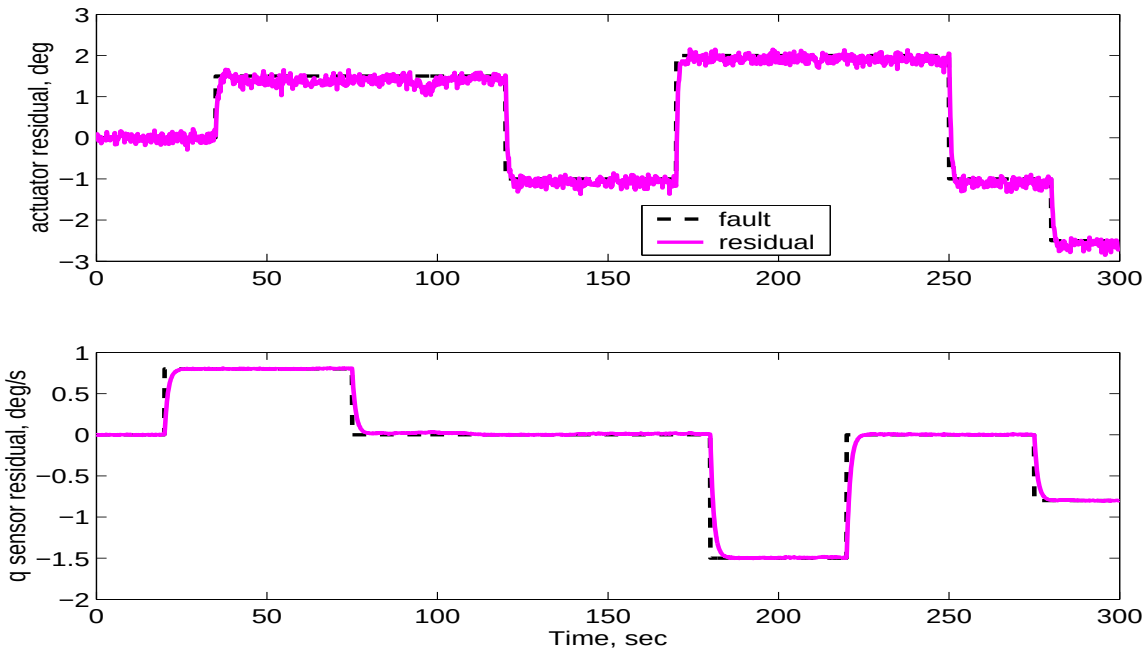

Figure 8. Residuals: nonlinear closed loop, moderate gust/noise (trim point 5).

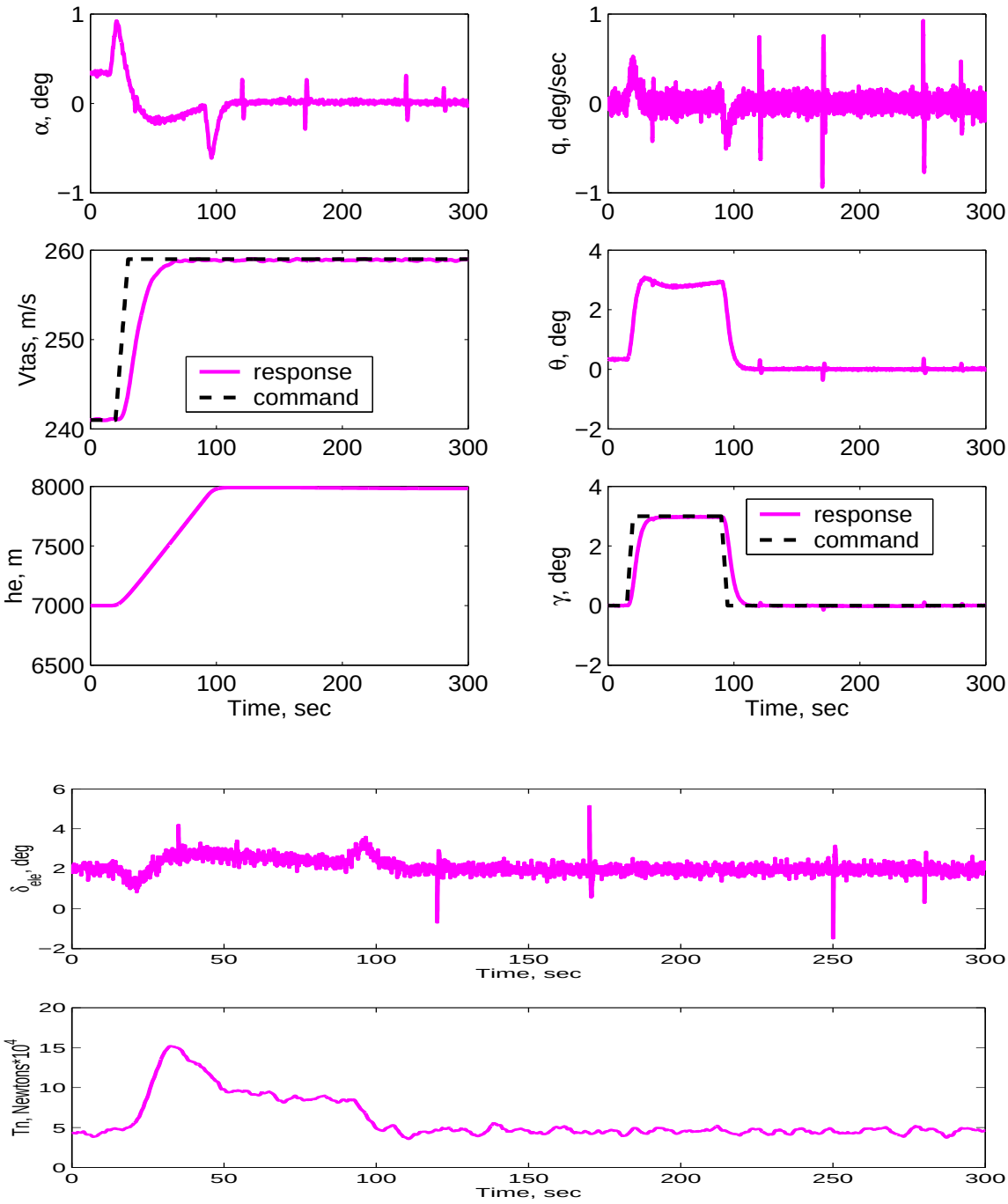

Figure 9. Plant responses & inputs: nonlinear closed loop, moderate gust/noise (trim point 5).

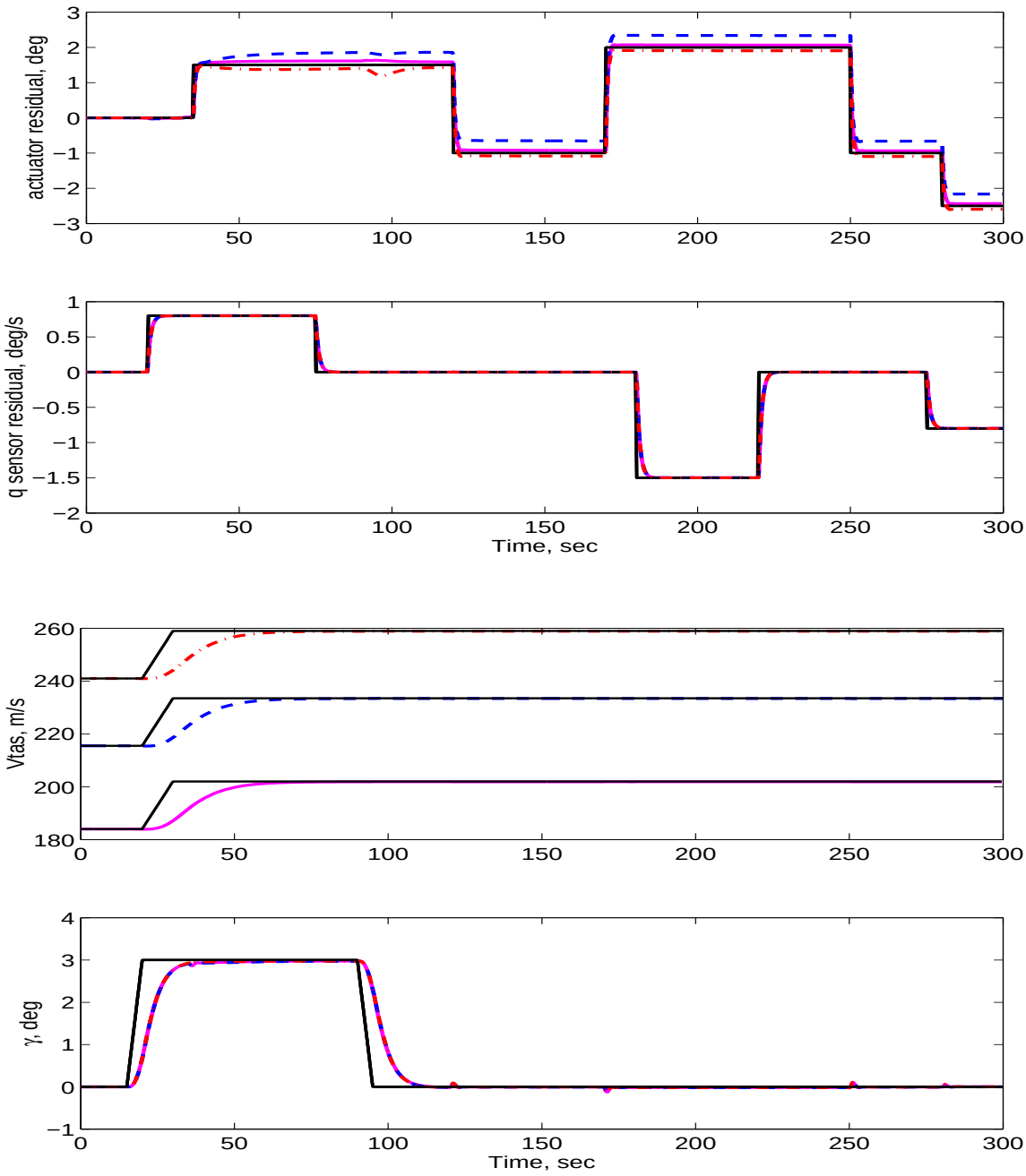

Figure 10. Nonlinear simulation: faults & control commands (thin solid), point 1 (thick solid), point 3 (thick dashed), point 5 (thick dashed-dot).

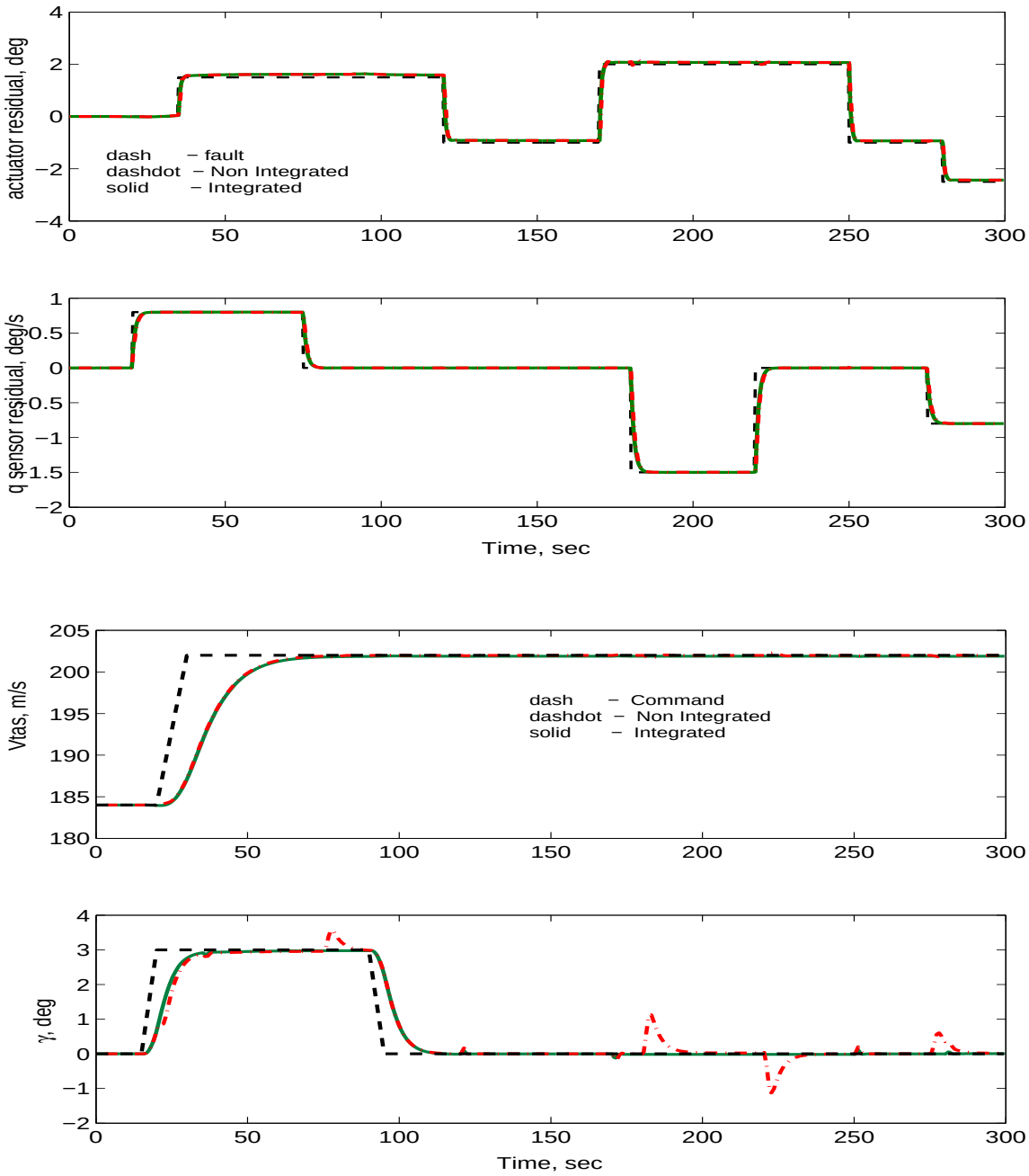

Figure 11. Residuals and commands nonlinear simulation: non-integrated and integrated comparison.

Table I. Trim points.

point	**altitude, m**	**airspeed, m/sec**	**Mach number**
1	4000	184	0.567
2	4000	232	0.71
3	9250	215.5	0.71
4	9250	247.75	0.81
5	7000	241	0.77